LaNi$_{1-x}$Co$_x$O$_3$ perovskites for application in electrochemical reactions involving molecular oxygen

J.X. Flores-Lasluisa [a], F. Huerta [b], D. Cazorla-Amorós [c], E. Morallón [a],[*]

[a] *Dept. Química Física e Instituto Universitario de Materiales, Universidad de Alicante, Ap. 99, E-03080, Alicante, Spain*
[b] *Dept. Ingenieria Textil y Papelera, Universitat Politecnica de Valencia, Plaza Ferrandiz y Carbonell, 1. E-03801, Alcoy, Spain*
[c] *Dept. Química Inorgánica e Instituto Universitario de Materiales, Universidad de Alicante, Ap. 99, E-03080, Alicante, Spain*

ABSTRACT

LaNi$_{1-x}$Co$_x$O$_3$ perovskite materials were synthesized by a sol-gel method for use in electrochemical reactions which involve molecular oxygen. The metal oxides were characterized by different physicochemical techniques and it was observed that the incorporation of Co induces some changes in the surface of the materials that affect the electrocatalytic activity. The different perovskite metal oxides were mixed with carbon black (Vulcan) to improve their electrocatalytic performance. The results from TPR and TPD techniques supported the XPS interpretation suggesting that a stronger interaction between carbon material and metal oxides can be obtained by physically mixing the two materials. This interaction improves the electron transfer and enhances the catalytic activity. Among the as-prepared materials, it was observed that the electrocatalytic performance of LaNi$_{1-x}$Co$_x$O$_3$ perovskite/Vulcan materials is higher than that of LaNiO$_3$/Vulcan for ORR, but similar towards OER. It is claimed that Co^{3+} is more catalytic for ORR, while Ni^{3+} favors the OER. Moreover, the presence of Co stimulates the formation of chemisorbed oxygen species, which also favor the electron transfer. Metal oxides containing both cations show higher stability, being this effect more notorious for OER. LaNi$_{0.5}$Co$_{0.5}$O$_3$/Vulcan seems a suitable bifunctional catalyst for both electrochemical reactions.

1. Introduction

The depletion of fossil fuels together with the environmental problems associated to their use has intensified the search for alternative, cleaner, and more sustainable energy sources. However, the complete replacement of fossil fuels is not feasible without adequate reduction in cost, efficient energy storage, and optimal integration of smart grid energy supply. Then, it is necessary to develop systems capable of storing energy when production from renewable sources exceeds demand and releasing it into the opposite case. In this context, hydrogen fuel cells, metal-air batteries, and electrolyzers appear as promising devices to meet future energy requirements [1,2]. However, two of the electrochemical reactions involved in these devices, the oxygen reduction reaction (ORR) and the oxygen evolution reaction (OER), exhibit slow reaction kinetics which makes necessary the use of electrocatalysts to increase the reaction rate [3,4]. At present, the most extended materials for this purpose are based on scarce and expensive metals such as platinum for ORR [5,6] and iridium or ruthenium for OER [7]. Designing new catalysts with a lower economic cost is then essential to

develop these electrochemical technologies.

One of the most studied properties of new catalysts is their bifunctional character which, inspired by the selectivity of enzymatic catalysis, arises from specific chemical interactions with the reactants. In this context, perovskite-based metal oxide materials are expected to play a key role in the future for both ORR and OER reactions, due to the possibility of tailoring their chemical composition and physicochemical properties [8–11]. In particular, lanthanum-based perovskites of general formula LaBO$_3$, where B is a 3d transition metal cation, were reported to serve as bifunctional catalysts for ORR and OER [12–14]. In these materials, moderate interactions between surface B-site cations and oxygen-containing intermediates are required for good performance towards both electrochemical reactions [15,16]. It is also known that higher catalytic activity can be reached when the B-cation e_g orbital fills with approximately one electron and an increase of the B–O bond covalency occurs [17].

Acting as a B cation, cobalt provides the catalyst with improved bifunctionality and stability under ORR and OER working conditions [13,18]. In addition, recent studies demonstrated that the partial

substitution of cobalt by manganese, to form LaMn$_{1-x}$Co$_x$O$_3$ structures, yields even better performance due to the synergistic effect of both metals [19–21]. By using nickel instead of cobalt, one can obtain the LaNiO$_3$ perovskite which provides, on the one hand, more covalent B–O bonds thanks to the presence of Ni^{3+}/Ni^{2+} redox couple and, on the other, additional oxygen vacancies resulting in higher electronic conductivity. In fact, the OER reaction is faster on LaNiO$_3$ but this material shows poor activity towards ORR [22–25]. To overcome this problem, some researchers proposed the use of a combination of cobalt and nickel in B sites [26–29]. Certainly, as it was expected, nickel substitution in LaCoO$_3$ enhanced the electrocatalytic activity towards OER [26,28] but the LaNiO$_3$ perovskite could still show higher performance under certain conditions [27].

Perovskite metal oxides are generally poor electrical conductors, a feature that limits their catalytic activity in electrochemical reactions. However, by mixing the catalyst with suitable conducting substrates, a better overall catalytic response can be achieved. Carbon-based materials such as carbon black or carbon nanotubes are interesting options due to their low price, high surface area and high electrical conductivity [30–33]. They are known to catalyze the ORR reaction through a two-electron transfer pathway but, unfortunately, they do not exhibit any activity towards OER [33,34]. In the modified mechanism for ORR, peroxide produced at the carbon support decomposes on the perovskite oxides surface, thus favoring the reduction of oxygen [35]. For OER, the O$_2$ produced on the perovskite surface seems to undergo spillover onto the carbon material surface which, in practice, results in a higher number of available perovskite active sites [36]. Several groups reported a synergistic effect between perovskite and carbon materials that increases the activity towards both reactions [21,37,38]. It was also suggested that a strong interaction between both components can be generated, which results in an enhanced electron transfer during electrochemical reactions. For materials consisting of metal oxides in situ synthesized at carbon materials, such an interaction was deduced from electrochemical results [37,38]. Usually XPS is the technique chosen to demonstrate the existence of this kind of interaction by a shift in the signal XPS of the cation spectra [34,39,40], however this shift could be due to the presence of carbon material that has an electronegative character. Thus, to support XPS results complementary characterization techniques should be applied.

In the present work, we report the synthesis of bifunctional electrocatalysts for ORR and OER based on the general formulation LaNi$_{1-x}$Co$_x$O$_3$. The physicochemical properties of these perovskite metal oxides materials will be characterized by employing microscopic, spectroscopic and diffraction techniques. The perovskite oxides materials will be mixed with carbon black (Vulcan XC-72R) to improve both electrical conductivity and electrochemical performance. Moreover, TPR and TPD experiments in combination with XPS analysis will be employed to confirm the existence of a strong interaction between metal oxides and carbon materials.

2. Experimental

2.1. Materials and reagents

Reagents used in this work were lanthanum (III) nitrate hexahydrate (La(NO$_3$)$_3$·6H$_2$O) (Sigma-Aldrich, 99.99%), nickel (II) nitrate hexahydrate (Ni(NO$_3$)$_2$·6H$_2$O) (Merck, ACS reagent), cobalt (II) nitrate hexahydrate (Co(NO$_3$)$_2$·6H$_2$O) (Sigma-Aldrich, ACS reagent), citric acid (Sigma-Aldrich 99%), ethylenediaminetetraacetic acid (EDTA) (Sigma-Aldrich, ACS reagent) and ammonia (NH$_3$) (VWR Chemicals, analytic reagent). All these chemicals were used with no further purification.

Moreover, commercial Vulcan XC-72R carbon black (Vulcan) (Cabot Corporation), potassium hydroxide (KOH) (VWR Chemicals), isopropanol 99.5% (Acros. Organics), Nafion® 5% w/w water and 1-propanol (Alfa Aesar) and 20 wt% Pt/C (Sigma-Aldrich) were also used. The solutions were prepared using ultrapure water (18 MΩ cm from a

Millipore Milli-Q system) and the gases, N$_2$ (99.999%), O$_2$ (99.995%) and H$_2$ (99.999%) were provided by Air Liquide and were used without any further treatment.

A commercial Pt (20 wt%) on graphitized carbon (Sigma-Aldrich) was used as an ORR reference electrocatalyst (Pt/C), whereas a commercial Ti mesh electrode coated with IrO$_2$ (Magneto, The Netherlands) was used for OER reference (IrO$_2$/Ti).

2.2. Synthesis procedure

LaNi$_{1-x}$Co$_x$O$_3$ perovskites (x = 0, 0.3, 0.5, 0.7, and 1) were synthesized by the modified sol-gel method described previously [41]. The mass of reagents was adjusted to obtain 1.0 g of product, employing a 2:3:1:1 M ratio for EDTA, citric acid, La(NO$_3$)$_3$·6H$_2$O and the sum of Ni (NO$_3$)$_2$·6H$_2$O and Co(NO$_3$)$_2$·6H$_2$O, respectively. First, EDTA was dissolved in a mixture of 41 mL deionized water and 3.3 mL NH$_3$. The metal precursors and citric acid were added to the EDTA solution. NH$_3$ was slowly dropped into the solution to set the pH at 9 to form a stable sol complex. Then, the solution was stirred at 80 °C for 6 h and subsequently dried at 150 °C for 12 h in the stove. Then, the sample was heated at 500 °C for 30 min until a fluffy product was obtained. Finally, this product was ground and calcined at 700 °C for 6 h to form the perovskite metal oxide material. Each LaNi$_{1-x}$Co$_x$O$_3$ perovskite was physically mixed with Vulcan in a 50 wt% concentration using an agate mortar for 10 min until a homogenous material was formed, thus obtaining the LaNi$_{1-x}$Co$_x$O$_3$/Vulcan catalysts.

2.3. Physicochemical characterization

Perovskite materials were characterized by X-ray diffraction (XRD) employing Cu Kα radiation source at a step of 0.05° in the 2θ range from 10° to 80° on a Bruker D8 Advance diffractometer (Billerica, USA) with Goebel (non-planar samples) with high-temperature Chamber (up to 900 °C) with an X-ray generator KRISTALLOFLEX K 760-80F (power: 3000 W, voltage: 20–60 KV and current:5–80 mA). The Scherrer equation was applied to estimate the crystallite sizes [42]:

$$D_c = \frac{k\lambda}{\beta \cos(\theta)} \tag{1}$$

where D$_c$ is the crystallite size (nm); k is the constant associated to the grain shape that has a value of 0.89; λ is the wavelength of the radiation source used whose value is 0.15406 nm; β corresponds to the full width at half maximum (FWHM) (radians), and θ is the Bragg angle. To correct the instrumental broadening factor from the measured FWHM value, a crystalline quartz pattern was used. The following equation was applied to calculate the corrected FWHM value of the sample [43]:

$$\beta_{real}^2 = \beta_{obs}^2 - \beta_{inst}^2 \tag{2}$$

where β_{real} is a value obtained only from the crystal size, β_{obs} is the measured value, and β_{inst} is the value associated with the instrument obtained from the quartz pattern.

The perovskite metal oxides and those mixed with carbon black were characterized by X-ray photoelectron spectroscopy (XPS) in a VG-Microtech Multilab 3000 equipment (Thermo-Scientific, Waltham, MA, USA), equipped with an Al Kα radiation source (1253.6 eV). XPSPEAK41 software was used to deconvolute the XPS data; experimental curves were adjusted by a combination of Lorentz-Gaussian functions and a Shirley line was used as the background.

The morphologies and microstructures of the samples were characterized by scanning electron microscopy (SEM, Hitachi S–3000 N, Chiyoda, Japan). Then, the freshly synthesized perovskite powders were covered by a thin layer of gold. Transmission electron microscopy (TEM, JEOL-2010, 200 kV accelerating voltage, Akishima, Japan) has been also used. The bulk composition of the perovskites was analyzed by energy-dispersive X-ray spectroscopy (EDX) with an X-ray detector device

attached to the SEM.

The surface area of perovskite oxides and perovskite/Vulcan materials was obtained by physical adsorption of N_2 (−196 °C) using an automatic adsorption system Autosorb-6 and an Autosorb Degasser from Quantachrome Instruments. Before the adsorption, the samples were outgassed at 250 °C under vacuum for 8 h. The nitrogen adsorption data were used to calculate Brunauer-Emmett-Teller (BET) surface area values.

Temperature-programmed desorption (TPD) measurements were performed to get information about the interaction between the carbon material and the metal oxides. The samples were heated up to 920 °C at a heating rate of 20 °C/min under a helium flow rate of 100 mL/min. The experiments were performed in a thermogravimetric system (TA Instruments, SDT Q600 Simultaneous) coupled to a mass spectrometer (PRISMA PRO QMG 250 M). The amounts of CO and CO evolved during the experiments were quantified by calibration of the 28 and 44 m/z signals using calcium oxalate.

In addition, the perovskite oxides and perovskite/Vulcan materialswere analyzed by temperature-programmed reduction (TPR) (5 vol % H_2 in Ar (35 mL/min), 10 °C/min up to 950 °C) employing a Micromeritics Pulse Chemisorb 2705 with a thermal conductivity detector (TCD) (Norcross, GA, USA).

2.4. Electrochemical characterization

To electrochemically characterize the samples, an ink was prepared by sonicating a suspension containing 1 mg of the material and 1 mL of a solution composed of 20 vol% isopropanol, 80 vol% water and 0.02 vol % Nafion®. The electrochemical measurements were done at 25 °C (using a thermostatic bath) in a three-electrode cell in 0.1 M KOH medium using an Autolab PGSTAT302 (Metrohm, Netherlands). A rotating ring-disk electrode (RRDE) from Pine Research Instruments (USA), equipped with a glassy carbon (GC) disk (5.61 mm diameter) and a Pt ring was used as a working electrode. A graphite rod was used as a counter electrode and a reversible hydrogen electrode (RHE) immersed in the working electrolyte as a reference electrode and all the potentials are referred to this electrode.

120 μL of the dispersion were deposited on the glassy carbon disk and a uniform catalyst layer of 480 μg/cm^2 of active material was obtained. Cyclic voltammetry (CV) and linear sweep voltammetry (LSV) experiments were performed. The ORR was studied by LSV experiments using different rotation rates between 400 and 2025 rpm at 5 mV s^{-1} from 1 to 0 V (vs RHE) in 0.1 M KOH solution. The Pt ring electrode potential was kept at 1.5 V during all the measurements. The electron transfer number, n_{e^-}, was calculated from the hydrogen peroxide oxidation at the Pt ring electrode, according to Ref. [19]:

$$HO_2^-[\%] = 200x \frac{I_{ring}/N}{I_{disk} + I_{ring}/N} \tag{3}$$

$$n_{e^-} = \frac{4I_{disk}}{I_{disk} + I_{ring}/N} \tag{4}$$

where I_{disk} and I_{ring} are the current measured at disk and ring electrodes, respectively, and N is the collection efficiency of the ring electrode that was experimentally determined as 0.37. To study the electroactivity of samples in OER, LSV experiments were performed from 1 to 1.8 V in an N_2-saturated atmosphere using a rotation rate of 1600 rpm at 5 mV s^{-1} in 0.1 M KOH.

3. Results and discussion

3.1. Surface structure and composition

Porous catalytic materials are preferred because the diffusion of reactants and products is facilitated, and they also provide a higher

amount of active sites for electrochemical reactions. The method employed for the synthesis of LaNi$_{1-x}$Co$_x$O$_3$ perovskites is expected to favor the formation of porosity [19]. The surface of perovskites was examined by SEM, which revealed a fairly similar morphology: irregular globular structures formed by small particles of variable size, around 200 nm, which appear aggregated forming pores of different dimensions, as can be observed in Fig. 1Sa. Since the bulk and surface composition of perovskite metal oxides may differ noticeably [41], XPS was applied for an appropriate chemical characterization of the surface. In addition, such a technique allows distinguishing oxidation states at the surface B-site cations, which play a significant role in electrochemical reactions involving molecular oxygen.

Fig. 1 displays XPS spectra in La 3d, Co 2p, Ni 2p, and O 1s regions for a set of perovskite samples at increasing cobalt substitution levels. The La 3d spectrum (Fig. 1a) is characterized by two well-separated signals at 833.1 eV and 849.9 eV that split into two contributions. The two main signals are associated with La 3d$_{5/2}$ and La 3d$_{3/2}$, respectively, while the 16.8 eV spin-orbit splitting suggests a trivalent valence state for lanthanum [44]. The spectrum of Co 2p (Fig. 1b) displays two asymmetric peaks at about 779.6 eV and 794.7 eV, which are attributed to Co 2p$_{3/2}$ and Co 2p$_{1/2}$, respectively. It is known that Co^{2+} and Co^{3+} show similar binding energies, but the elucidation of the main cobalt species is based on two facts. On the one hand, the spin-orbit splitting, which is close to 15 eV, suggests Co^{3+} as the main surface oxidation state. On the other hand, it is known that visible satellites appear usually at about 785 eV for Co(II) containing compounds. So, the lack of features in this region supports the prevalence of Co^{3+} at the perovskite metal oxide surface [45,46]. The Ni 2p core-level spectrum is shown in Fig. 1c, which is characterized by a low intensity Ni 2p$_{1/2}$ signal at 871.7 eV and a more intense Ni 2p$_{3/2}$ feature at 854 eV. The latter overlaps with the La 3d$_{3/2}$ signal, making it difficult to isolate the contributions coming from Ni^{2+} and Ni^{3+} species. This can be done however from the main Ni 2p$_{3/2}$ signal or using the Ni 2p$_{1/2}$ satellite at around 865 eV [47–49]. Finally, Fig. 1d shows the shift of the O 1s signal from 528.3 eV up to 528.7 eV as the cobalt substitution is increased. This phenomenon is related to the number of electrons in the $3d$ orbital, which can affect the electron density around O. In this case, Co has fewer electrons than Ni which produces a lower back-bonding effect to O, thus the progressive introduction of Co increases the binding energy [50].

For a more accurate evaluation of the different oxidation states at perovskite B sites, XPS spectra are deconvoluted as presented in Fig. 2 and quantified in Table 1. The main Co 2p$_{3/2}$ and Co 2p$_{1/2}$ signals can be easily separated into two peaks corresponding to (II) and (III) redox states: Co^{2+} (781.3 and 796.5 eV) and Co^{3+} (779.6 and 794.7 eV) [26, 28]. The Ni 2p$_{3/2}$ signal was separated into two contributions at 871.6 and 873.1 eV, which can be associated with Ni^{2+} and Ni^{3+}, respectively [47,51]. Furthermore, the deconvolution of Ni 2p$_{1/2}$ satellite into peaks at 862.2 and 865.3 eV supports the presence of these two oxidation states [47,52]. Finally, four peaks are identified for O 1s, being the peaks at 528.4 and 529.1 related to lattice oxygen (O$_L$) in lanthanum oxide and B-site oxide, respectively. While the peaks at 530.9 and 532.4 eV correspond to surface chemisorbed oxygen species (O$_C$) and adsorbed water (O$_W$) [53,54].

Table 1 shows atomic ratios obtained for A and B cations and oxygen species. As the first column shows, lanthanum predominates at the surface of all samples, but a surface depletion of this species occurs as cobalt is introduced. Interestingly, the B species that replaces lanthanum at the surface is predominantly cobalt, as deduced from its higher atomic ratio against its nominal value. In particular, the surface enriches in Co^{3+} species over Co^{2+} at increasing cobalt substitution. The effect is the opposite for nickel, the other B-cation, whose predominant oxidation state at the surface is Ni^{2+}. Such a behavior differs from that reported for LaMn$_{1-x}$Co$_x$O$_3$ perovskites [41], for which high cobalt-substitution levels seemed to stimulate the surface enrichment of B cations in their respective higher oxidation states (Mn^{4+} and Co^{3+} against Mn^{3+} and Co^{2+}). The concentration and nature of surface cations govern the
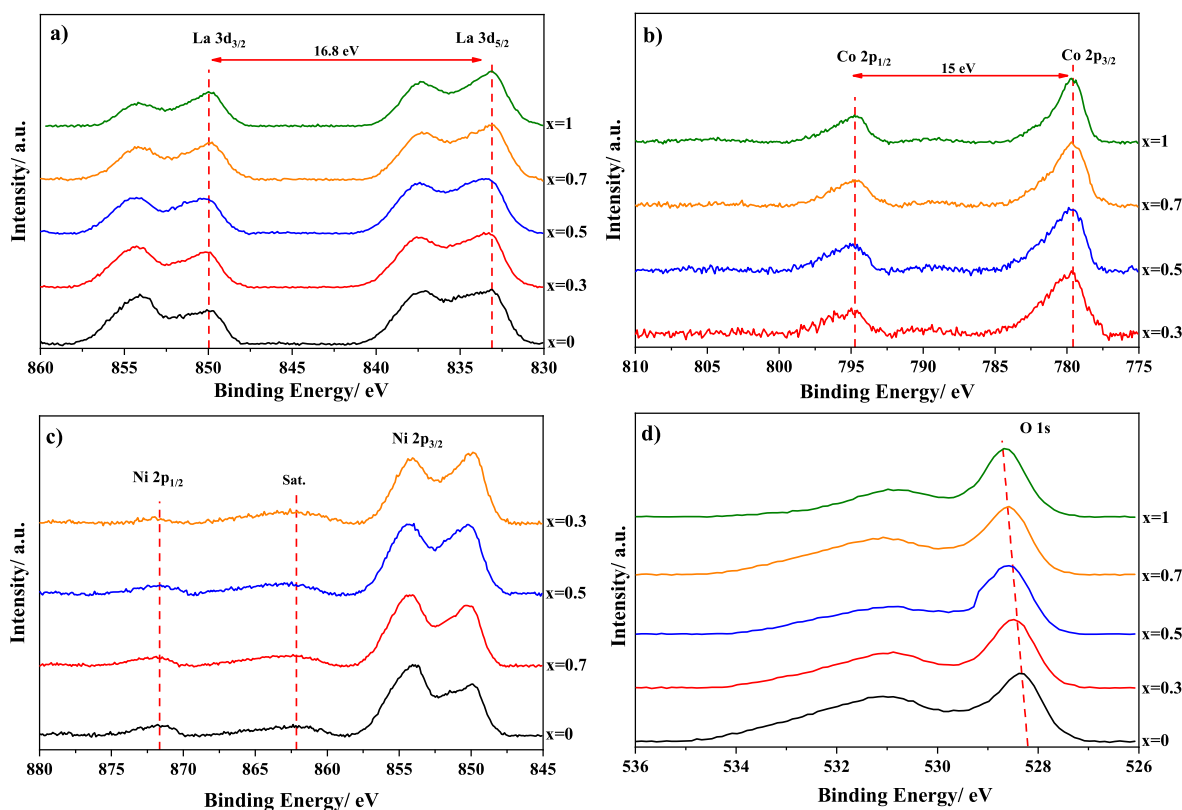
Fig. 1. X-ray photoelectron signals obtained from **(a)** La 3d; **(b)** Co 2p; **(c)** Ni 2p and **(d)** O 1s spectral regions for different LaNi$_{1-x}$Co$_x$O$_3$ perovskites.
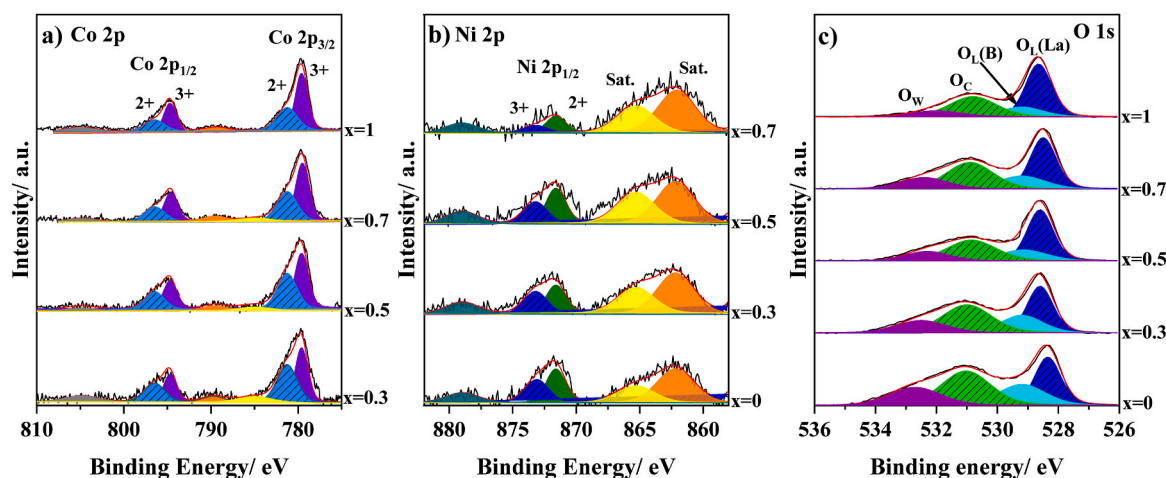

Fig. 2. Deconvolution of XPS signals of: **(a)** Co 2p; **(b)** Ni 2p and **(c)** O 1s for a set of LaNi$_{1-x}$Co$_x$O$_3$ perovskites.

Table 1
Atomic ratios obtained after deconvolution of XPS from data in Fig. 3.

Sample	$\frac{Ni + Co}{La}$	$\frac{Ni}{Ni + Co}$	Co 2p Co^{3+}/Co^{2+}	Ni 2p Ni^{3+}/Ni^{2+}	O 1s O$_C$/O$_{L(B)}$
LaNiO$_3$	0.28	1.00	–	0.8	1.9
LaNi$_{0.7}$Co$_{0.3}$O$_3$	0.37	0.54	0.9	1.0	1.9
LaNi$_{0.5}$Co$_{0.5}$O$_3$	0.46	0.53	1.1	0.8	2.0
LaNi$_{0.3}$Co$_{0.7}$O$_3$	0.45	0.20	1.3	0.6	2.2
LaCoO$_3$	0.46	0.00	1.6	–	2.8

formation of surface oxygen species, which in turn affects the catalytic performance. Among the detected oxygen species, the high content of chemisorbed oxygen can improve the electrocatalytic activity of the perovskite materials. The chemisorbed oxygen species are related to surface hydroxyls [55] that are occupying the position of missing lattice oxygen. For this reason, many studies have related these chemisorbed oxygen species to oxygen vacancies produced on the surface due to the B-cations being surrounded only by 5 oxygen anions rather than 6 [56]. Moreover, these surface hydroxyl groups play an important role in the electrochemical reaction mechanisms that will be explained later.

To understand better the positive effect of chemisorbed oxygen species, the ratio of chemisorbed and lattice oxygen was calculated (although only the lattice oxygen at B-site oxide was considered because

of its lower surface concentration and relevance in the mechanisms of electrocatalytic reactions). Table 1 shows that $O_C/O_L(B)$ ratio increases at higher cobalt content and, accordingly, it can be deduced that the presence of cobalt supports the formation of chemisorbed oxygen species, i.e., the oxygen vacancy formation. These vacancies enhance the electrical conductivity and increase the covalency of the B–O bond, resulting in better electrocatalytic performance [20,57].

3.2. Bulk structure and composition

Among the factors influencing the activity of electrocatalysts, particle size and other structural parameters are both of critical importance. Small particle size provides more accessible active sites, which results in better catalytic performance. TEM microscopy was employed to characterize the morphology of perovskite metal oxides and the results are presented in Fig. 1S. Nanoparticles are apparently of polyhedral shape, with an average size that increases from 30 nm, for the unsubstituted $LaNiO_3$ perovskite, up to 60 nm after complete cobalt substitution, $LaCoO_3$. The replacement of nickel by cobalt has also an effect on the microstructure, as deduced from the lower particle agglomeration shown at increasing cobalt levels.

The bulk composition of the metal oxides was characterized by SEM-EDX mapping and the results revealed that cations are homogeneously dispersed in the material, with no phase segregation detected, as can be observed in Fig. 2S for $LaNi_{0.5}Co_{0.5}O_3$ perovskite. As the crystal structure plays a significant role in the metal oxides electroactivity, the $LaNi_{1-x}Co_xO_3$ materials were characterized by X-ray diffraction technique and the XRD patterns are displayed in Fig. 3. The $LaNiO_3$ diffractogram shows peaks at 2θ values close to 23°, 33°, 41°, 47°, 59° and 69° that can be indexed to a rhombohedral hexagonal $LaNiO_3$ belonging to the space group R-3c ($LaNiO_3$, PDF code: 96-100-0310). Diffraction peaks coming from La_2O_3, $La(OH)_3$ or Co_3O_4 impurities were not detected. On the contrary, the appearance of small peaks at 2θ values close to 37°, 43°, and 63° indicates that there is a small nickel (II) oxide impurity in the diffractogram of $LaNiO_3$ (x = 0, black curve) [25]. This minor component results from the use of a too low calcination temperature, as temperatures higher than 750 °C are required to obtain pure perovskite phases [27]. In this case, mild calcination temperatures were preferred to circumvent an increase in crystallite size of the cobalt-based lanthanum perovskite oxides [58]. Partially substituted $LaNi_{1-x}Co_xO_3$ perovskites, with x = 0.3, 0.5, and 0.7, are indexed to a rhombohedral hexagonal $LaNiO_3$, with no detection of NiO impurities in these samples. Finally, the $LaCoO_3$ diffractogram (x = 1, green curve) shows peaks at 2θ

values close to 23°, 33°, 41°, 47°, 59° and 69° that can be indexed to a rhombohedral hexagonal $LaCoO_3$ belonging to the space group R-3c ($LaCoO_3$, PDF code: 96-153-3634) [28].

Fig. 4b shows the magnified XRD signal in the region of 46°-48° corresponding to the (024) plane of the rhombohedral hexagonal structure. An increase in the cobalt level has two effects. Firstly, the diffraction peak shifts slightly towards a higher angle, which suggests a progressive cell contraction. Secondly, the signal becomes narrower. It can be then concluded that the crystallinity of these materials seems to be positively influenced by higher cobalt content. The lattice parameters can be obtained from Bragg's equations [43]:

$$d = \frac{\lambda}{2 \sin \theta} \tag{5}$$

$$\frac{1}{d^2} = \frac{4}{3} \frac{(h^2 + hk + k^2)}{a^2} + \frac{l^2}{c^2} \tag{6}$$

where d is the interplanar distance, (hkl) are the Miller indices corresponding to the interplanar distance and a and c are the lattice parameters. The average crystal size was calculated using the Scherrer equation for angles at 22°-23° and 47°-48°. The mean crystallographic values obtained from the XRD data are summarized in Table 2. The effect of cobalt substitution is twofold. On the one hand, it results in an enlargement of the crystallite size and, on the other hand, it promotes a lattice contraction due to the lower ionic radius of Co^{3+} (0.52 Å) versus Ni^{3+} (0.58 Å) [26,59].

The BET specific surface area of perovskite oxides and perovskite/Vulcan catalysts was determined by N_2 adsorption isotherms at −196 °C and the results are listed in Table 2. As expected, perovskite metal oxides materials exhibit quite a low BET surface area. The BET surface area of Vulcan is about 255 m^2 g^{-1}, and those obtained for the perovskite/Vulcan samples agree with the mixtures rule [60]. The $LaNi_{0.5}Co_{0.5}O_3$/Vulcan sample shows a slightly higher surface area that could provide better electrochemical properties than the other materials. This hypothesis will be tested in the next section.

3.3. Electrochemical characterization

From the electrochemical characterization of unsubstituted $LaCoO_3$ and $LaCoO_3$/Vulcan catalysts (Fig. 3S), it can be concluded that the presence of carbon material is essential to enhance the electrochemical behavior of perovskites. This is mainly (but not exclusively, as it will be explained later) due to an increase in electrical conductivity [21].
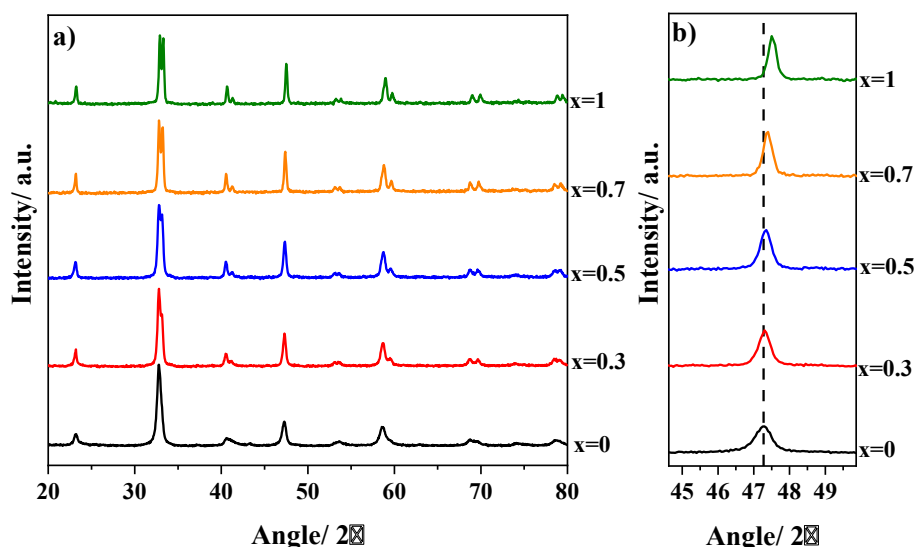

Fig. 3. (a) X-ray diffraction patterns for a set of $LaNi_{1-x}Co_xO_3$ perovskites at the increasing level of Co-substitution and (b) zoom in the diffraction line at 47°.

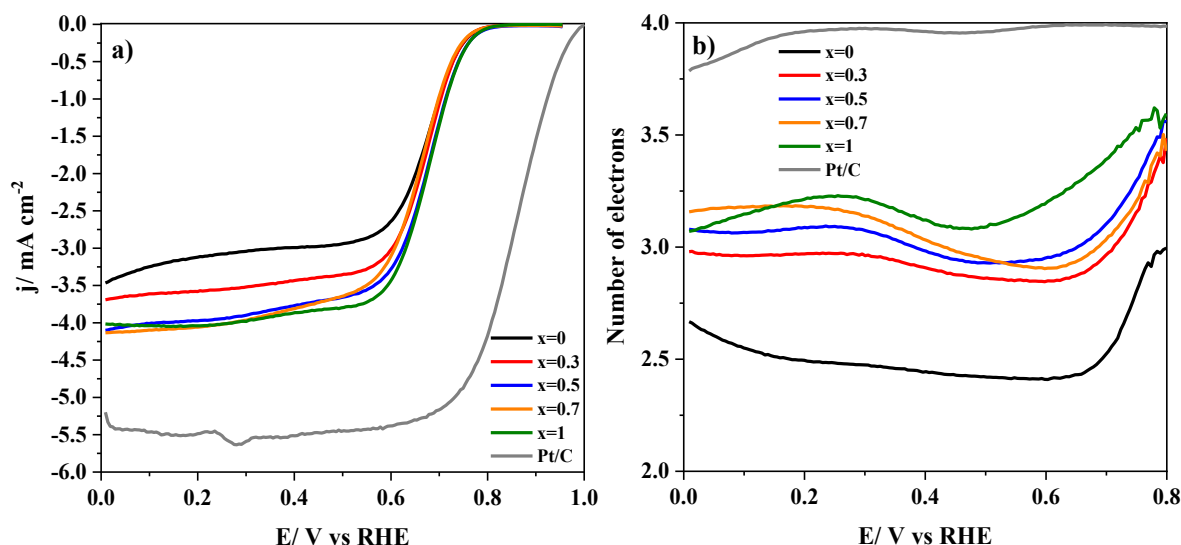**Fig. 4.** **a)** RDE linear sweep voltammograms for $LaNi_{1-x}Co_xO_3$/Vulcan and 20%Pt/C in 0.1 M KOH solution saturated with O_2 at 1600 rpm, v = 5 mV s^{-1}; **b)** Number of electrons transferred in ORR at increasing potential as obtained from Eq. (2) by using the current measured at the ring electrode.

Table 2
Average crystallite size, lattice parameters and unit cell volume for $LaNi_{1-x}Co_xO_3$ perovskites obtained from XRD patterns. BET surface area obtained from N_2 isotherms.

Sample	Crystallite size (nm)	Lattice parameters		Lattice volume (Å^3)	BET/m^2 g^{-1}	
		a	c		Perovskite	Perovskite/Vulcan
$LaNiO_3$	17	5.464	13.161	392.949	14	118
$LaNi_{0.7}Co_{0.3}O_3$	27	5.464	13.142	392.325	13	118
$LaNi_{0.5}Co_{0.5}O_3$	27	5.458	13.155	391.925	18	125
$LaNi_{0.3}Co_{0.7}O_3$	49	5.459	13.105	390.467	13	114
$LaCoO_3$	55	5.443	13.090	387.794	13	119

Several electrochemical parameters, such as the double layer capacitance, current density, electrochemical activity or selectivity (especially for ORR) are enhanced in the presence of carbon material. As the cobalt substitution level influences the physicochemical properties of $LaNi_{1-x}Co_xO_3$ perovskites, it is expected that the electrochemical response of these catalysts can be also modified and their performance, in terms of ORR and OER, can be modulated.

$LaNi_{1-x}Co_xO_3$/Vulcan were first characterized by cyclic voltammetry in 0.1 M KOH solutions saturated with either N_2 or O_2 (the results can be seen in Fig. 4S). The unsubstituted $LaNiO_3$/Vulcan (black curve) and the fully substituted $LaCoO_3$/Vulcan (green curve) display significant differences related to the redox activity of the B-site cation. The voltammetric peaks at 0.65 V/0.33 V are ascribed to the Ni(II)/Ni(III) redox process [61,62], whereas redox processes involving cobalt are not observed for $LaCoO_3$/Vulcan within the potential window of the voltammogram. As a result, increasing the cobalt content in $LaNi_{1-x}Co_xO_3$ materials causes a progressive vanishing of nickel redox peaks on the voltammetric curves. It is worth noting that the voltametric charge of $LaNi_{0.5}Co_{0.5}O_3$/Vulcan is higher than expected, an effect that could be connected to the higher BET surface area of this material. In the presence of dissolved O_2 (Fig. 4Sb) the CV for all samples show a sharp cathodic peak at around 0.7 V, which is related to oxygen reduction reaction. This electrochemical process will be studied by means of the RRDE technique to obtain representative electrochemical parameters of the reaction.

The ORR activity was tested by LSV recorded at 1600 rpm in 0.1 M KOH medium saturated with O_2 and the results are depicted in Fig. 4a. These samples show almost identical onset potentials but different limiting current densities. The number of electrons transferred in the electrochemical reaction is depicted in Fig. 4b, from which a range of 2.4–3.6 is found. The unsubstituted $LaNiO_3$ sample (black curve) seems

the less selective material for the 4-electron reaction pathway. In fact, nickel redox states are more active for producing hydrogen peroxide than for the direct reduction of the oxygen molecule to hydroxide. To compare the electroactivity of the as-prepared materials, a commercial 20%Pt/C was tested. As was expected, it has a great activity and selectivity for 4-electron pathway, however, it is cost and expensive and shows lower activity for OER in comparison with other electrodes like IrO_2.

The 4-electron pathway is the most effective mechanism for ORR because it produces the highest power and avoids the formation of corrosive peroxide species [63]. At perovskite metal oxides materials this reaction involves four steps, which include the interaction of surface B-site cations and oxygen-containing species, that is, surface hydroxide displacement, surface peroxide formation, surface oxide formation and surface hydroxide regeneration (see a detailed mechanism described in the supporting information from Eq. (5S) to Eq. 8S). The first and the last one appear as rate-determining steps, Eq. S5 and Eq. S8 respectively [15, 64]. As reported [21,65], the interaction of perovskite metal oxides and carbon materials causes a synergistic effect on ORR. The carbon material component plays two main roles: to improve the electrical conductivity and to act as a co-catalyst, by supplying HO_2^- species to the perovskite for further reduction to hydroxide [35,65]. Table 3 summarizes the electrochemical parameters obtained for all samples from Fig. 4. For the limiting current density parameter, we selected the potential 0.4 V because above this potential both materials work in the ORR simultaneously. At lower potential not only the reduction of the oxygen but also the reduction of the peroxide is produced as it can be observed from pure perovskite (Fig. 3Sc). Thus, the influence of carbon material might be more prominent for the reduction of oxygen species rather than perovskite oxides at lower potentials. According to this, $LaNiO_3$/Vulcan seems

Table 3

Onset potential, number of electrons transferred, and limiting current density obtained for ORR reaction at LaNi$_{1-x}$Co$_x$O$_3$/Vulcan materials.

Sample	E_{onset}/V (at −0.10 mA cm^{-2})	n_{e^-} (at 0.7 V)	j_{lim}/mA cm^{-2} (at 0.4 V)	Tafel slope/ mV dec^{-1}	ECSA/ cm^2
LaNiO$_3$/Vulcan	0.77	2.53	−2.99	63	4.5
LaNi$_{0.7}$Co$_{0.3}$O$_3$/ Vulcan	0.77	2.97	−3.44	61	3.3
LaNi$_{0.5}$Co$_{0.5}$O$_3$/ Vulcan	0.79	3.11	−3.77	64	3.8
LaNi$_{0.3}$Co$_{0.7}$O$_3$/ Vulcan	0.77	3.04	−3.81	64	3.0
LaCoO$_3$/Vulcan	0.78	3.40	−3.87	59	3.3
20% Pt/C	0.98	3.99	−5.51	60	–

the less active material for ORR with lower onset potential, current density and number of transferred electrons, a characteristic attributed to the lower catalytic performance of Ni compared to other 3d metals such as Mn or Co [12,13,66]. As a consequence of the higher activity of Co^{3+} compared to Ni^{3+}, the electrocatalytic activity of samples increases with the concentration of cobalt. Apart from the surface concentration of cobalt, the O$_C$/O$_{L(B)}$ ratio increases at higher cobalt contents, thus proving that the presence of the surface hydroxyl groups affects positively the ORR performance. In addition, the fact that Co^{3+} has a better e_g orbital filling than Ni^{3+} facilitates the charge transfer in the surface hydroxide displacement step (the first stage in ORR mechanism), which results in an improved ORR performance [57]. However, the electrocatalytic activity not only depends on this parameter, but nanoparticles size can also influence in the activity, being strongly recommendable to have small nanoparticles for a great catalytic activity. The nanoparticle size could influence in the electrochemical surface area (ECSA) shown in Table 3 (the detailed protocol and calculation is provided in supporting information, Fig. 5S). For example LaNi$_{0.3}$Co$_{0.7}$O$_3$/Vulcan has the lowest ECSA value which can be related to a large nanoparticle size. Thus, despite of having a higher cobalt content and Co^{3+} species, it catalytic performance is lower than LaNi$_{0.3}$Co$_{0.7}$O$_3$/Vulcan due to the higher particle size and lower ECSA value.

Partially substituted LaNi$_{1-x}$Co$_x$O$_3$/Vulcan materials show Tafel slopes slightly above 60 mV dec^{-1}, which are similar to those reported in literature (Fig. 6Sa) [13,22,67]. The stability of materials with x = 0.5, 0.7 and 1 was studied under ORR conditions by chronoamperometry. The experiments were carried out on an RRDE at 1600 rpm and 0.65 V in an O$_2$-saturated 0.1 M KOH medium. Results were compared against a commercial 20%Pt/C material and, additionally, tolerance to methanol was tested by adding this compound 3 h after the experiment started (Fig. 5). As expected, the platinum-based material (black curve) exhibits long-term stability with a 5% loss of current after 180 min. However, after methanol addition, the recorded current drops to almost zero due to the poisoning of the active metal. The behavior of LaNi$_{1-x}$Co$_x$O$_3$/Vulcan materials is quite similar prior to methanol addition (up to 10% decrease of the initial activity). On the contrary, these samples exhibit higher methanol tolerance than Pt-based electrocatalysts as deduced from the minor loss of activity (an additional 5–10%) detected in the presence of this alcohol. Among the LaNi$_{1-x}$Co$_x$O$_3$/Vulcan materials, the ones with both cations exhibit slightly better stability due to the presence of two different redox pairs, which can make it easier to maintain electroneutrality avoiding the structure collapse.

We shall examine now the OER reaction at perovskite/Vulcan materials, which can proceed over two different pathways depending on the applied potential [36]. At low overpotential, the peroxide generated through a 2-electron step from hydroxide can disproportionate into oxygen and hydroxide (Eq. (3S)). At high overpotential, the mechanism involves 4 steps, as in ORR but in the reverse direction (see the mechanism described from Eq. 9S to Eq. 12S): surface oxide formation, surface hydroperoxide formation, deprotonation of the hydroperoxide
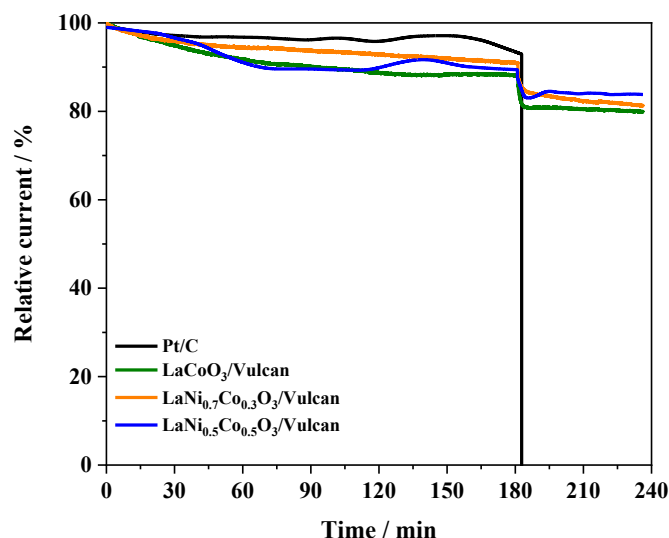

Fig. 5. Comparative stability test for LaNi$_{1-x}$Co$_x$O$_3$/Vulcan and 20% Pt/C carried out at 0.65 V and 1600 rpm in O$_2$-saturated 0.1 M KOH at 25 °C and tolerance to methanol added 180 min after the experiment started (final alcohol concentration: 1 M).

group to form peroxide and the replacement of O$_2$ by surface hydroxide. The two intermediate stages are rate-determining i.e., Eq.10S and Eq. 11S, respectively [16]. Vulcan undergoes oxidation at lower potentials to those required for OER. Thus, when combined with perovskite metal oxides, its main role consists on liberating catalytic sites at the active component through the spillover of oxygen [22,30].

An RRDE was employed to examine the electrocatalytic activity of LaNi$_{1-x}$Co$_x$O$_3$ perovskite/Vulcan materials towards OER in an alkaline medium and the results are presented in Fig. 6. Moreover, the commercial IrO$_2$/Ti electrode was tested to compared with the as-prepared materials. Those materials with lower cobalt substitution exhibit anodic peaks at 1.35–1.45 V that can be associated with the oxidation of Ni^{2+} to Ni^{3+} prior to the eventual OER [26]. The onset potential for OER slightly increases at increasing cobalt levels and, consequently, the best material for this reaction would be LaNiO$_3$/Vulcan. A similar result can be deduced from the volcano plot reported by Bockris et al. [68]. As
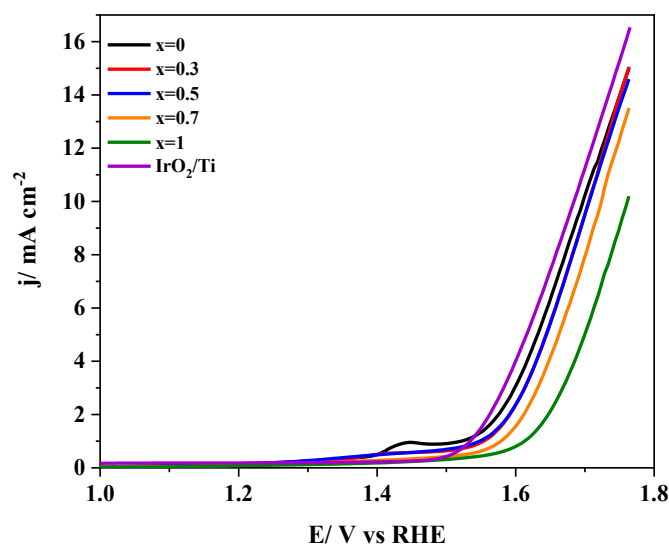

Fig. 6. Linear sweep voltammograms recorded for OER at 1600 rpm at LaNi$_{1-x}$Co$_x$O$_3$/Vulcan materials and IrO$_2$/Ti mesh electrode in 0.1 M KOH medium saturated with N$_2$. Scan rate 5 mV s^{-1}.

expected, the commercial electrocatalyst shows the best response for OER, but the activity of the as-prepared materials was quite close. This makes them promising electrocatalysts for such a reaction. Although oxygen vacancies reinforce the covalency of the B–O bond, which promotes charge transfer between surface B-site cations and oxygen intermediate species [23], they seem not to affect substantially the overall activity in OER. The nature of B-site cation seems a more significant parameter and, obviously, Ni^{3+} is the preferred species.

Tafel slopes measured for OER at partially substituted materials are lower than those obtained for single Ni or Co perovskites (Fig. 6Sb). That means that the electron transfer kinetics can be substantially better on those samples. Slopes close to 120 mV dec^{-1} show that the surface hydroxide displacement is the electron transfer determining step of the process [67]. Despite that $LaNi_{0.3}Co_{0.7}O_3$/Vulcan has smaller Tafel slope than $LaNiO_3$/Vulcan, the overall reaction kinetics for $LaNiO_3$/Vulcan is faster due to the higher ECSA and Ni^{3+} concentration making this material the best for OER.

A proper method to evaluate the bifunctionality of $LaNi_{1-x}Co_xO_3$/Vulcan materials for ORR and OER involves the analysis of ΔE, the difference between E_{j10}^{OER} and E_{j-1}^{ORR} (which is the ORR potential recorded at -1.0 mA cm^{-2}). This has been done in Table 4, where smaller ΔE values represent improved bifunctional electrochemical performance. The best bifunctionality corresponds to the half-substituted sample, $LaNi_{0.5}Co_{0.5}O_3$/Vulcan, which shows ΔE values similar to noble-metal benchmark materials (1.16 V for 20% Pt/C and 0.92 for 20% Ir/C [54]) or to other perovskite-based materials such as $La_{0.8}Sr_{0.2}Mn_{0.6}Ni_{0.4}O_3$ ($\Delta E = 1.074$ V) [23], $LaNiO_3$-nanorod/reduced graphene oxide ($\Delta E = 1.0775$ V) [25], $LaMn_{0.7}Co_{0.3}O_3$ ($\Delta E = 1.19$ V) [19], $La_{0.6}Sr_{0.4}CoO_{3-\delta}$ ($\Delta E = 1.13$ V) [36], and $LaCoO_3$/N-doped reduced graphene oxide ($\Delta E = 1.02$ V) [18]. It should be noted that some previous studies reported even lower values for perovskite oxide hybrid materials: $La(Co_{0.55}Mn_{0.45})_{0.99}O_{3-\delta}$ nanorod/graphene ($\Delta E = 0.96$ V) [69], $LaMn_{0.9}Co_{0.1}O_3$/N-doped CNT ($\Delta E = 0.96$ V) [32] and encapsulated $LaNiO_3$/N-doped CNT ($\Delta E = 0.79$ V) [38]. However, all of them were synthesized by in situ methods, which are more complex than the one presented in this work.

In addition to the analysis of stability under ORR conditions, a comprehensive characterization of bifunctional catalysts should also include stability and durability tests for OER. Both chronoamperometry [70] and cyclic voltammetry [18] techniques can be used for this purpose. In this case, we employed low scan rate in the CV experiments to test Ni-containing samples, as they exhibit better electrocatalytic performance. The potential was swept from 1.0 to 1.8 V at 5 mV s^{-1} and the current at 1.75 V on the forward scans was recorded. Fig. 7 shows how the current decreases during the first 20 consecutive potential cycles. Although $LaNiO_3$/Vulcan exhibited the best response for OER, Fig. 8 reveals its low stability, as the oxygen production drops by 80% at the end of the experiment. Indeed, the stability of materials is clearly enhanced after cobalt incorporation with, typically, more than 80%

Table 4
Electrochemical parameters obtained from $LaNi_{1-x}Co_xO_3$/Vulcan materials under OER and ORR conditions: Potential required to obtain 10 mA cm^{-2} in OER, Tafel slope for OER, Potential required to obtain -1.0 mA cm^{-2} in ORR and bifunctional electrocatalytic activity.

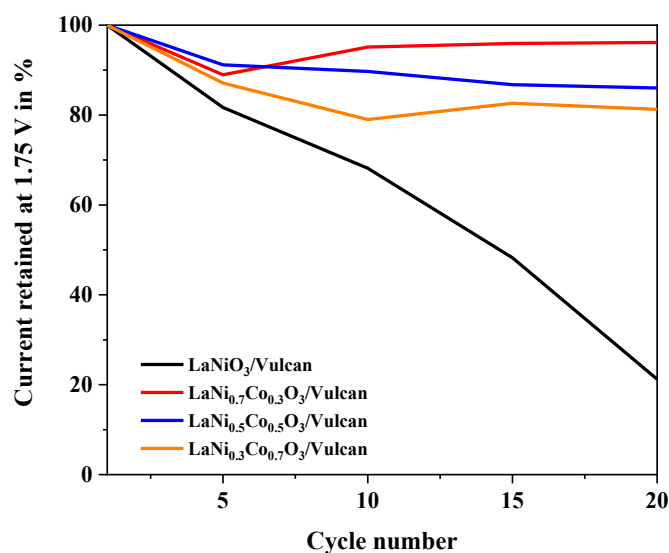| Sample	E_{j10}^{OER}/V	OER Tafel slope/ mV dec^{-1}	E_{j-1}^{ORR}/V	ΔE/V ($E_{j10}^{OER} - E_{j-1}^{ORR}$)
$LaNiO_3$/Vulcan	1.70	136	0.71	0.99
$LaNi_{0.7}Co_{0.3}O_3$/ Vulcan	1.71	120	0.72	0.99
$LaNi_{0.5}Co_{0.5}O_3$/ Vulcan	1.71	126	0.73	0.98
$LaNi_{0.3}Co_{0.7}O_3$/ Vulcan	1.73	110	0.71	1.01
$LaCoO_3$/Vulcan	1.76	160	0.73	1.03
IrO_2/Ti	1.68	89	–	–

Fig. 7. Stability of $LaNi_{1-x}Co_xO_3$/Vulcan samples as revealed by the current retained at 1.75 V during OER experiments. See text for more details.
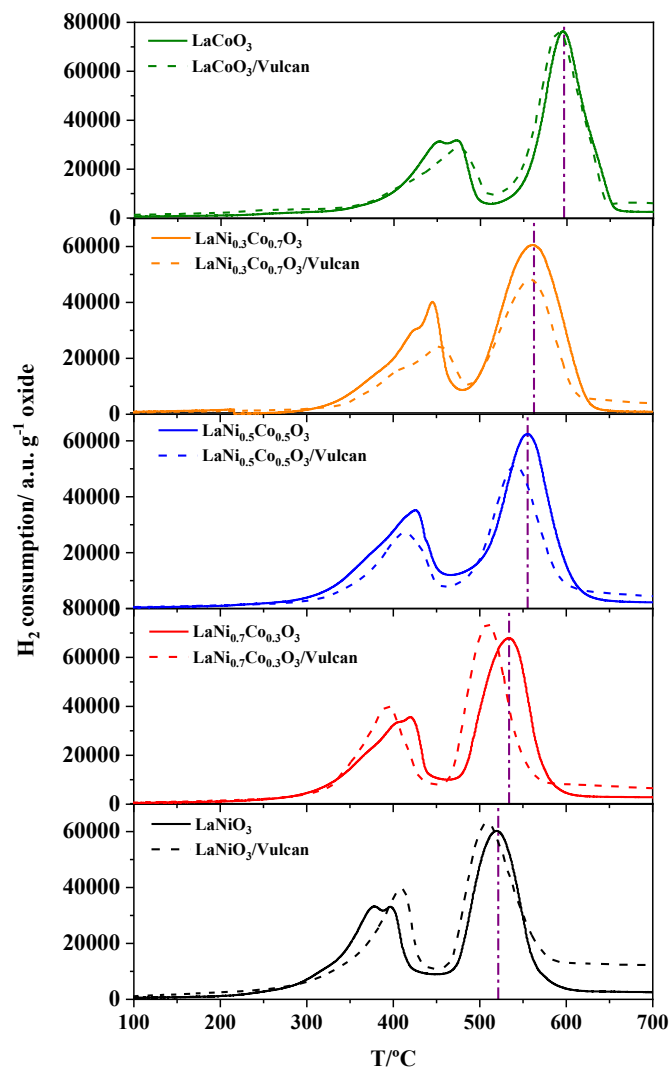

Fig. 8. Temperature Programmed Reduction (TPR) profiles for the $LaNi_{1-x}Co_xO_3$ materials (solid line) and $LaNi_{1-x}Co_xO_3$/Vulcan materials (dashed line) displaying the H_2 consumption by grams of metal oxide.

current retained. The higher crystallinity induced by cobalt seems to be at the origin of the lower degradation detected for these samples, with no significant differences found between them. Hence, the presence of cobalt seems to be necessary for the proper operation of these materials under OER conditions.

3.4. Interaction between the B-site cation and carbon material

Previous studies [34,39,40] have reported on the importance of the in situ synthesis of metal oxide/carbon materials to generate a covalent bond between the B-site cation and carbon to enhance the electron transfer and, consequently, the overall reaction. However, it was also reported [21] that a physical mixing may generate a strong interaction between both materials that could enhance the ORR performance. In the present context, additional characterization tools are required to prove the existence of such interaction between $LaNi_{1-x}Co_xO_3$ and Vulcan and to gain more insight on its true nature. The experimental techniques selected to achive this purpose were temperature programmed reduction (TPR) and temperature programmed desorption (TPD). Both are quite sensitive to measure reducibility and gas desorption from metal oxides with (and without) carbon material. In this way, Fig. 8 displays the TPR profiles of $LaNi_{1-x}Co_xO_3$ (solid lines) and $LaNi_{1-x}Co_xO_3$/Vulcan (dashed lines) materials. All materials have two well-differentiated regions related to different reduction processes [53,59,71]. The pure $LaNiO_3$ perovskite has one region related to the reduction of Ni^{3+} to Ni^{2+} (200–450 °C) and a the second one related to the reduction of Ni^{2+} to Ni^0 between (450–650 °C). Whereas for the $LaCoO_3$ perovskite, both regions appear at higher temperatures; the first region at 200–510 °C includes the reduction of Co^{3+} to Co^{2+} and the second region at 510–700 °C the reduction of Co^{2+} to Co^0. Therefore, in the metal oxide materials that
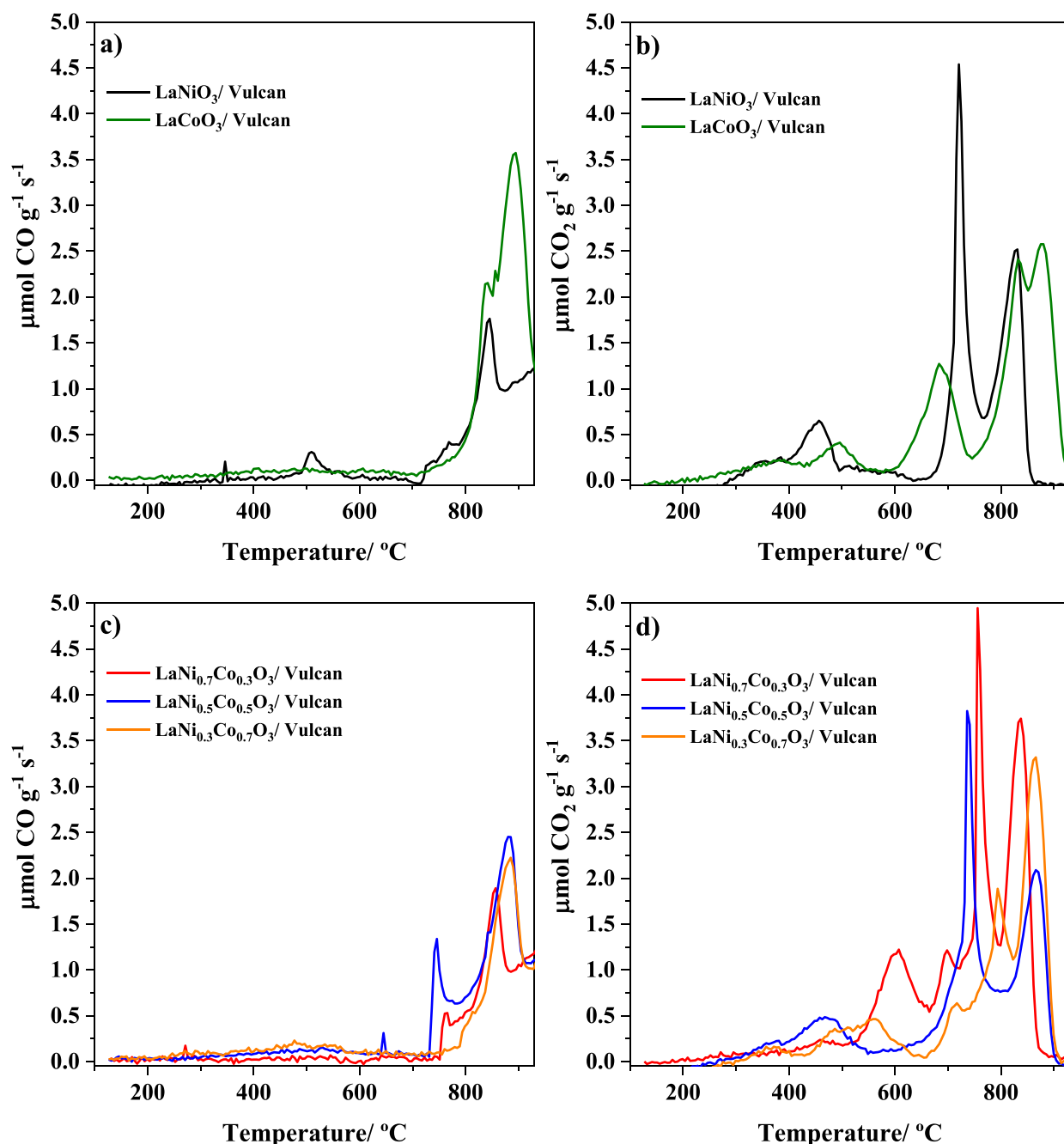

Fig. 9. a) CO and b) CO_2 TPD profiles of $LaNi_{1-x}Co_xO_3$/Vulcan materials.

contain both cations, there is a progressive shift from the temperature range of the $LaNiO_3$ perovskite to the one of $LaCoO_3$ perovskite. In these cases, both regions are related to the reduction processes of nickel and cobalt species.

Before analyzing the $LaNi_{1-x}Co_xO_3$/Vulcan samples, the Vulcan material was studied by TPR technique observing a low hydrogen consumption; thus, the carbon material does not contribute significantly to the reduction processes observed in the TPR. Fig. 8 displays the TPR profiles of the $LaNi_{1-x}Co_xO_3$/Vulcan referred to the mass of metal oxides (dashed lines), for a proper comparison with the pure metal oxides profiles. The results show a similar hydrogen consumption profile compared to pure perovskite materials. However, the presence of carbon black produces some changes in the reduction temperature of the $LaNi_{1-x}Co_xO_3$/Vulcan materials, which are more relevant with increasing the Ni content. As it can be observed in the second reduction region, there is a shift to lower temperatures in the presence of carbon material. Thus, the reducibility of the $LaNi_{1-x}Co_xO_3$/Vulcan increases in comparison to the pure perovskite samples. These results indicate that there is an interaction between both materials produced by the physical mixing, affecting positively the electrochemical performance [21]. However, the shift in the temperature depends on the cobalt content, at low cobalt substitution ($0.3 \leq x \leq 0.5$) the shift is higher, whereas at high cobalt content ($0.7 \leq x \leq 1$) the shift is almost negligible.

At this point TPD was applied to confirm the existence of strong interaction after physical mixing. First, $LaNi_{1-x}Co_xO_3$ (x = 0, 0.5, and 1) and Vulcan materials were characterized individually (see Fig. 7S). As expected, carbon black shows low content of surface oxygen groups. Perovskite metal oxide materials show low content of surface oxygen groups, desorbing mainly as CO_2 which is related to surface carbonate species [72,73]. From the studied perovskite metal oxides, the material with both Ni and Co cations seems to have the ability to form a higher amount of carbonate species due to the synergistic effect between both metal cations.

Fig. 9 displays the CO and CO_2 profiles for the $LaNi_{1-x}Co_xO_3$/Vulcan materials showing that the combination of both materials generates large CO and CO_2 formation. In carbon materials, the desorption of these gases are related to the decomposition of surface oxygen groups [74]. However, in the metal oxide/carbon composites the large amount of CO and CO_2 must be the due to the carbothermal reduction reaction of the metal oxide by the carbon material that occurs at high temperatures [75]. This reaction might be favoured by the strong interaction between the perovskite metal oxide and the carbon material through the C–O–B bond. It is clearly observed differences in desorption profiles of the $LaNi_{1-x}Co_xO_3$/Vulcan materials, especially, for the CO_2 TPD profiles. The materials with high Ni content show a sharp desorption peak at around 700–800 °C, which tends to decrease its intensity and almost combine with the signal at around 800–900 °C with decreasing the Ni

content, as can be observed from the $LaCoO_3$/Vulcan material. This indicates the higher reactivity of Ni-based materials with the carbon material at a lower temperature, which might not be caused by the strength of the interaction between both components, but due to the nickel species properties.

Table 5 presents the results of the quantification of the oxygen-containing compounds determined from the TPD experiments. Moreover, the total amount of oxygen desorbed from the surface and lattice oxygen species according to the desorption temperature is also shown. The surface oxygen is related to species such as adsorbed carbonates, water and hydroxyls, thus only the contribution of CO_2 and H_2O profiles, at temperatures below 600 °C, are considered for its calculation. As it can be observed for Vulcan-containing materials the amount of surface oxygen species increases. Thus, it seems that the procedure employed for the synthesis of the mixed materials generates surface oxygen species, which might be adsorbed over new available B-site cations, which can participate and enhance the overall electrochemical reactions. The desorption of CO and CO_2 related to the lattice oxygen removal (calculated by subtracting the surface oxygen to the total amount of oxygen desorbed) might be the result of the reaction between the metal oxide and the carbon material. As it can be observed, this value is almost half of the theoretical oxygen content in the metal oxide. This suggests that the perovskite metal oxide material is preferentially reduced at the interphase between both materials where there is a more intimate contact. Moreover, observing the values of the lattice oxygen, all the samples exhibit a similar value, indicating that the interaction between both the metal oxide and carbon material is quite similar for all materials regardless of the B-site cation. Thus, the mechanical energy provided during the physical mixing seems to be enough to produce an interaction between both materials. We can observe that the final desorption temperature of both gases increases with the cobalt content, thus, the thermal stability of the material is affected by the cobalt substitution; we can corroborate this with the enthalpy of formation of pure $LaNiO_3$ and $LaCoO_3$ having the latter a higher value [76].

To further corroborate the results from TPR and TPD experiments, $LaNi_{1-x}Co_xO_3$/Vulcan materials were analyzed using X-ray photoelectron spectroscopy (XPS) and compared to $LaNi_{1-x}Co_xO_3$ oxides. The O 1s and Co 2p spectra are presented in Fig. 8S to observe any possible changes in the binding energies as a result of the interaction. In this case, the Ni 2p spectra are not included because they are very noisy to observe any change.

Fig. 8Sa shows the O 1s spectra of the metal oxides mixed with Vulcan compared to the Vulcan spectrum. The carbon black exhibits two peaks at around 532.2 and 533.6 eV which are related to the oxygen bonds C=O, and C–O and O–C=O, respectively [77]. Regarding the $LaNi_{1-x}Co_xO_3$/Vulcan samples, two main peaks at around 528.5 and 532.3 eV can be distinguished, being the former related to the lattice

Table 5

TPD quantification of the $LaNi_{1-x}Co_xO_3$ (x = 0, 0.5, and 1), Vulcan and $LaNi_{1-x}Co_xO_3$/Vulcan materials. Moreover, the theoretical O concentration per gram of oxide material is shown in the Table.

Sample	μmol H_2O/g	μmol CO/g	μmol CO_2/g	Experimental (μmol O/g)		Theoretical lattice (μmol O/g)
				[a]Surface	[b]Lattice	
Vulcan	211	257	184	836		–
$LaNiO_3$	338	154	132	547	209	12215
$LaNi_{0.5}Co_{0.5}O_3$	562	151	704	1034	1087	12209
$LaCoO_3$	349	166	165	650	195	12203
$LaNiO_3$/Vulcan	1150	712	1070	1287	2715	6108
$LaNi_{0.7}Co_{0.3}O_3$/Vulcan	1020	581	1550	1225	3476	6106
$LaNi_{0.5}Co_{0.5}O_3$/Vulcan	1230	862	1160	1381	3031	6105
$LaNi_{0.3}Co_{0.7}O_3$/Vulcan	1240	688	1210	1393	2955	6103
$LaCoO_3$/Vulcan	889	1050	1230	981	3418	6102

[a] The determination of μmol O/g provided by the surface was calculated by summing the μmol of H_2O and CO_2 evolved until 600 °C. It is considered that under this temperature the surface components are evolved.

[b] The determination of μmol O/g provided by the lattice is the difference between the surface μmol O/g and the total concentration of μmol O/g evolved in each experiment.

oxygen species (O_L and O_B). The latter peak can be deconvoluted in four different contributions associated with the metal oxide, Vulcan and the possible interaction between both materials. The peak at 531 eV is related to surface chemisorbed oxygen species from the metal oxide material. The peaks at around 532 and 533.6 eV are related to the oxygen groups in the carbon material. Finally, the new peak at around 533.2 eV is associated with the C–O–B interaction produced between the carbon black and perovskite materials [39,40].

The interaction produced between both components can also be confirmed in the Co 2p spectra (Fig. 8Sb). The spectra show that there is a positive shift of around 0.5 eV, which can be associated with the interaction between both materials. This can result in a displacement of the electron cloud from the metallic cations to the lighter elements, thus increasing the binding energy in the cations [69]. This displacement was also observed in the O 1s spectra, where there is a negative shift of 0.2 eV (532 eV) in the mixed materials. Thus, both results support the existence of the C–O–B interaction between both components, which enhances the electrocatalytic performance of the materials due to the better electron transfer.

4. Conclusions

$LaNi_{1-x}Co_xO_3$ perovskites were successfully synthesized by a sol-gel method. An increase in the size of the crystallites as the cobalt content is increased has been observed. Besides, the presence of cobalt generates different oxidation states at B site cations, which positively participate in the reaction mechanisms.

Due to their low electrical conductivity and low active surface area, metal oxides should be mixed with carbon black to achieve better performance. The electrocatalytic response of $LaNi_{1-x}Co_xO_3$/Vulcan materials for ORR generally improves with increasing cobalt content due to the higher surface concentrations of Co^{3+} (a more active site) and O_{ads} (which favor the charge transfer). However, the samples containing both Co and Ni cations stand out over $LaCoO_3$/Vulcan in terms of stability and methanol poisoning.

On the other hand, $LaNi_{1-x}Co_xO_3$/Vulcan materials with higher nickel content exhibit better electrocatalytic performance for OER. Particularly, the response of $LaNiO_3$/Vulcan is better due to the highest surface concentration of Ni^{3+} supplied, which is the most active cation. However, it was found that little cobalt substitution results in an electrocatalytic behavior quite similar to that of $LaNiO_3$ and, in addition, provides better material stability while maintaining current density. Therefore, in terms of electrocatalytic activity, stability and bifunctionality, $LaNi_{0.5}Co_{0.5}O_3$/Vulcan shows the best compromise for ORR and OER. The combination of TPR and TPD experiments revealed significant changes in the reducibility and in the amount of CO and CO_2 evolved when carbon black is used. These observations together with the XPS data analysis strongly suggest that the strong interaction between carbon material and metal oxide is caused by the formation of C–O–B species, which enhance the electron transfer and, as a consequence, the overall reactions.

CRediT author statement

Authors contributed equally to this work.

Declaration of competing interest

The authors declare that they have no known competing financial interests or personal relationships that could have appeared to influence the work reported in this paper.

Data availability

Data will be made available on request.

Appendix A. Supplementary data

Supplementary data to this article can be found online at https://doi.org/10.1016/j.energy.2023.127256.

References

[1] Abas N, Kalair A, Khan N. Review of fossil fuels and future energy technologies. Futures 2015;69:31–49. https://doi.org/10.1016/j.futures.2015.03.003.

[2] Olabi AG, Wilberforce T, Abdelkareem MA. Fuel cell application in the automotive industry and future perspective. Energy 2021;214:118955. https://doi.org/10.1016/j.energy.2020.118955.

[3] Li M, Bi X, Wang R, Li Y, Jiang G, Li L, et al. Relating catalysis between fuel cell and metal-air batteries. Matter 2020;2:32–49. https://doi.org/10.1016/j.matt.2019.10.007.

[4] Banham D, Ye S. Current status and future development of catalyst materials and catalyst layers for proton exchange membrane fuel cells: an industrial perspective. ACS Energy Lett 2017;2:629–38. https://doi.org/10.1021/acsenergylett.6b00644.

[5] Marković NM, Schmidt TJ, Stamenković V, Ross PN, Li YY, Li YY, et al. Oxygen reduction reaction on Pt and Pt bimetallic surfaces: a selective review. Fuel Cell 2001;134:105–16. https://doi.org/10.1002/1615-6854(200107)1:2<105::AID-FUCE105>3.3.CO;2-0.

[6] Chaisubanan N, Maniwan W, Hunsom M. Effect of heat-treatment on the performance of PtM/C (M = Cr, Pd, Co) catalysts towards the oxygen reduction reaction in PEM fuel cell. Energy 2017;127:454–61. https://doi.org/10.1016/j.energy.2017.03.162.

[7] Reier T, Oezaslan M, Strasser P. Electrocatalytic oxygen evolution reaction (OER) on Ru, Ir, and pt catalysts: a comparative study of nanoparticles and bulk materials. ACS Catal 2012;2:1765–72. https://doi.org/10.1021/cs3003098.

[8] Miao H, Wang Z, Wang Q, Sun S, Xue Y, Wang F, et al. A new family of Mn-based perovskite (La1-xYxMnO3) with improved oxygen electrocatalytic activity for metal-air batteries. Energy 2018;154:561–70. https://doi.org/10.1016/j.energy.2018.04.145.

[9] Flores-Lasluisa JX, Huerta F, Cazorla-Amorós D, Morallón E. Manganese oxides/LaMnO3 perovskite materials and their application in the oxygen reduction reaction. Energy 2022;247:123456. https://doi.org/10.1016/j.energy.2022.123456.

[10] Xu X, Wang W, Zhou W, Shao Z. Recent advances in novel nanostructuring methods of perovskite electrocatalysts for energy-related applications. Small Methods 2018;2:1800071. https://doi.org/10.1002/smtd.201800071.

[11] Wang H, Zhou M, Choudhury P, Luo H. Perovskite oxides as bifunctional oxygen electrocatalysts for oxygen evolution/reduction reactions – a mini review. Appl Mater Today 2019;16:56–71. https://doi.org/10.1016/j.apmt.2019.05.004.

[12] Sunarso J, Torriero AAJ, Zhou W, Howlett PC, Forsyth M. Oxygen reduction reaction activity of La-based perovskite oxides in alkaline medium: a thin-film rotating ring-disk electrode study. J Phys Chem C 2012;116:5827–34. https://doi.org/10.1021/jp211946n.

[13] Ashok A, Kumar A, Bhosale RR, Almomani F, Malik SS, Suslov S, et al. Combustion synthesis of bifunctional LaMO3 (M = Cr, Mn, Fe, Co, Ni) perovskites for oxygen reduction and oxygen evolution reaction in alkaline media. J Electroanal Chem 2018;809:22–30. https://doi.org/10.1016/j.jelechem.2017.12.043.

[14] Celorrio V, Dann E, Calvillo L, Morgan DJ, Hall SR, Fermin DJ. Oxygen reduction at carbon-supported lanthanides: the role of the B-site. Chemelectrochem 2016;3:283–91. https://doi.org/10.1002/celc.201500440.

[15] Suntivich J, Gasteiger HA, Yabuuchi N, Nakanishi H, Goodenough JB, Shao-Horn Y. Design principles for oxygen-reduction activity on perovskite oxide catalysts for fuel cells and metal–air batteries. Nat Chem 2011;3:546–50. https://doi.org/10.1038/nchem.1069.

[16] Suntivich J, May KJ, Gasteiger HA, Goodenough JB, Shao-Horn Y. A perovskite oxide optimized for oxygen evolution catalysis from molecular orbital principles. Science 2011;334(80):1383–5. https://doi.org/10.1126/science.1212858.

[17] Retuerto M, Pereira AG, Pérez-Alonso FJ, Peña MA, Fierro JLG, Alonso JA, et al. Structural effects of LaNiO3 as electrocatalyst for the oxygen reduction reaction. Appl Catal B Environ 2017;203:363–71. https://doi.org/10.1016/j.apcatb.2016.10.016.

[18] Liu K, Li J, Wang Q, Wang X, Qian D, Jiang J, et al. Designed synthesis of LaCoO3/N-doped reduced graphene oxide nanohybrid as an efficient bifunctional electrocatalyst for ORR and OER in alkaline medium. J Alloys Compd 2017;725:260–9. https://doi.org/10.1016/j.jallcom.2017.07.178.

[19] Liu X, Gong H, Wang T, Guo H, Song L, Xia W, et al. Cobalt-doped perovskite-type oxide LaMnO 3 as bifunctional oxygen catalysts for hybrid lithium-oxygen batteries. Chem Asian J 2018;13:528–35. https://doi.org/10.1002/asia.201701561.

[20] Hu J, Wang L, Shi L, Huang H. Oxygen reduction reaction activity of LaMn1-xCoxO3-graphene nanocomposite for zinc-air battery. Electrochim Acta 2015;161:115–23. https://doi.org/10.1016/j.electacta.2015.02.048.

[21] Flores-Lasluisa JX, Huerta F, Cazorla-Amorós D, Morallon E. Carbon material and cobalt-substitution effects in the electrochemical behavior of LaMnO3 for ORR and OER. Nanomaterials 2020;10:2394. https://doi.org/10.3390/nano10122394.

[22] Alexander CT, Abakumov AM, Forslund RP, Johnston KP, Stevenson KJ. Role of the carbon support on the oxygen reduction and evolution activities in LaNiO 3 composite electrodes in alkaline solution. ACS Appl Energy Mater 2018;1:1549–58. https://doi.org/10.1021/acsaem.7b00320.

[23] Wang Z, You Y, Yuan J, Yin YX, Li YT, Xin S, et al. Nickel-doped La 0.8 Sr 0.2 Mn 1-x Ni x O 3 nanoparticles containing abundant oxygen vacancies as an optimized bifunctional catalyst for oxygen cathode in rechargeable lithium-air batteries. ACS Appl Mater Interfaces 2016;8:6520–8. https://doi.org/10.1021/acsami.6b00296.

[24] Sakthivel M, Bhandari S, Drillet J-F. On activity and stability of rhombohedral LaNiO3 catalyst towards ORR and OER in alkaline electrolyte. ECS Electrochem Lett 2015;4. https://doi.org/10.1149/2.0081506eel. A56–8.

[25] Hu J, Liu Q, Shi Z, Zhang L, Huang H. LaNiO 3 -nanorod/graphene composite as an efficient bi-functional catalyst for zinc–air batteries. RSC Adv 2016;6:86386–94. https://doi.org/10.1039/C6RA16610E.

[26] Vignesh A, Prabu M, Shanmugam S. Porous LaCo 1– x Ni x O 3–δ nanostructures as an efficient electrocatalyst for water oxidation and for a zinc–air battery. ACS Appl Mater Interfaces 2016;8:6019–31. https://doi.org/10.1021/acsami.5b11840.

[27] Omari E, Makhloufi S, Omari M. Preparation by sol–gel method and characterization of Co-doped LaNiO3 perovskite. J Inorg Organomet Polym Mater 2017;27:1466–72. https://doi.org/10.1007/s10904-017-0604-y.

[28] Wang H, Xu W, Richins S, Liaw K, Yan L, Zhou M, et al. Polymer-assisted approach to LaCo1-xNixO3 network nanostructures as bifunctional oxygen electrocatalysts. Electrochim Acta 2019;296:945–53. https://doi.org/10.1016/j.electacta.2018.11.075.

[29] Samira S, Camayang JCA, Nacy AM, Diaz M, Meira SM, Nikolla E. Electrochemical oxygen reduction on layered mixed metal oxides: effect of B-site substitution. J Electroanal Chem 2019;833:490–7. https://doi.org/10.1016/j.jelechem.2018.12.023.

[30] Zhu Y, Zhou W, Shao Z. Perovskite/carbon composites: applications in oxygen electrocatalysis. Small 2017;13:1603793. https://doi.org/10.1002/smll.201603793.

[31] Kéranguéven G, Royer S, Savinova E. Synthesis of efficient Vulcan-LaMnO3 perovskite nanocomposite for the oxygen reduction reaction. Electrochem Commun 2015;50:28–31. https://doi.org/10.1016/j.elecom.2014.10.019.

[32] Lee DU, Park MG, Park HW, Seo MH, Ismayilov V, Ahmed R, et al. Highly active Co-doped LaMnO 3 perovskite oxide and N-doped carbon nanotube hybrid bi-functional catalyst for rechargeable zinc–air batteries. Electrochem Commun 2015;60:38–41. https://doi.org/10.1016/j.elecom.2015.08.001.

[33] Hu J, Wang L, Shi L, Huang H. Preparation of La1-xCaxMnO3 perovskite-graphene composites as oxygen reduction reaction electrocatalyst in alkaline medium. J Power Sources 2014;269:144–51. https://doi.org/10.1016/j.jpowsour.2014.07.004.

[34] Li T, Liu J, Jin X, Wang F, Song Y. Composition-dependent electro-catalytic activities of covalent carbon-LaMnO3 hybrids as synergistic catalysts for oxygen reduction reaction. Electrochim Acta 2016;198:115–26. https://doi.org/10.1016/j.electacta.2016.02.027.

[35] Mefford JT, Kurilovich AA, Saunders J, Hardin WG, Abakumov AM, Forslund RP, et al. Decoupling the roles of carbon and metal oxides on the electrocatalytic reduction of oxygen on La 1-x Sr x CoO 3-δ perovskite composite electrodes. Phys Chem Chem Phys 2019;21:3327–38. https://doi.org/10.1039/c8cp06268d.

[36] Mattick VF, Jin X, Yang T, White RE, Huang K. Unraveling oxygen electrocatalysis mechanisms on a thin-film oxygen-deficient perovskite La 0.6 Sr 0.4 CoO 3-δ. ACS Appl Energy Mater 2018;1:3937–46. https://doi.org/10.1021/acsaem.8b00669.

[37] Molina-García MA, Rees NV. Dual-doped graphene/perovskite bifunctional catalysts and the oxygen reduction reaction. Electrochem Commun 2017;84:65–70. https://doi.org/10.1016/j.elecom.2017.10.004.

[38] Lee DU, Park HW, Park MG, Ismayilov V, Chen Z. Synergistic bifunctional catalyst design based on perovskite oxide nanoparticles and intertwined carbon nanotubes for rechargeable zinc–air battery applications. ACS Appl Mater Interfaces 2015;7:902–10. https://doi.org/10.1021/am507470f.

[39] Liu J, Jin X, Song W, Wang F, Wang N, Song Y. Facile preparation of modified carbon black-LaMnO3 hybrids and the effect of covalent coupling on the catalytic activity for oxygen reduction reaction. Chin J Catal 2014;35:1173–88. https://doi.org/10.1016/S1872-2067(14)60066-8.

[40] Zhou J, Song H, Ma L, Chen X. Magnetite/graphene nanosheet composites: interfacial interaction and its impact on the durable high-rate performance in lithium-ion batteries. RSC Adv 2011;1:782. https://doi.org/10.1039/c1ra00402f.

[41] Flores-Lasluisa JX, Huerta F, Cazorla-Amorós D, Morallón E. Structural and morphological alterations induced by cobalt substitution in LaMnO3 perovskites. J Colloid Interface Sci 2019;556:658–66. https://doi.org/10.1016/j.jcis.2019.08.112.

[42] Zhu Y, Tan R. Preparation of nanosized LaCoO 3 perovskite oxide using amorphous heteronuclear complex as a precursor at low temperature. J Mater Sci 2000;5:5415–20. https://doi.org/10.1023/A:1004863332704.

[43] Waseda Y, Matsubara E, Shinoda K. X-ray diffraction crystallography, vol. 46. Berlin, Heidelberg: Springer Berlin Heidelberg; 2011. https://doi.org/10.1007/978-3-642-16635-8.

[44] Zhang C, Wang C, Zhan W, Guo Y, Guo Y, Lu G, et al. Catalytic oxidation of vinyl chloride emission over LaMnO3 and LaB0.2Mn0.8O3 (B=Co, Ni, Fe) catalysts. Appl Catal B Environ 2013;129:509–16. https://doi.org/10.1016/j.apcatb.2012.09.056.

[45] Okamoto Y, Nakano H, Imanaka T, Teranishi S. X-ray photoelectron spectroscopic studies of catalysts — supported cobalt catalysts. Bull Chem Soc Jpn 1975;48:1163–8. https://doi.org/10.1246/bcsj.48.1163.

[46] Gautier JL, Rios E, Gracia M, Marco JF, Gancedo JR. Characterisation by X-ray photoelectron spectroscopy of thin MnxCo3−xO4(1≥x≥0) spinel films prepared by low-temperature spray pyrolysis. Thin Solid Films 1997;311:51–7. https://doi.org/10.1016/S0040-6090(97)00463-X.

[47] Kim JK. PEG-Assisted sol-gel synthesis of compact nickel oxide hole-selective layer with modified interfacial properties for organic solar cells. Polymers 2019;11:120. https://doi.org/10.3390/polym11010120.

[48] Rida K, Peña MA, Sastre E, Martínez-Arias A. Effect of calcination temperature on structural properties and catalytic activity in oxidation reactions of LaNiO3 perovskite prepared by Pechini method. J Rare Earths 2012;30:210–6. https://doi.org/10.1016/S1002-0721(12)60025-8.

[49] Nie L, Wang J, Tan Q. In-situ preparation of macro/mesoporous NiO/LaNiO3 perovskite composite with enhanced methane combustion performance. Catal Commun 2017;97:1–4. https://doi.org/10.1016/j.catcom.2017.04.010.

[50] Zhao X, Yang Q, Cui J. XPS study of surface absorbed oxygen of ABO3 mixed oxides. J Rare Earths 2008;26:511–4. https://doi.org/10.1016/S1002-0721(08)60128-3.

[51] Mi L, Wei W, Huang S, Cui S, Zhang W, Hou H, et al. A nest-like Ni@Ni1.4Co1.6S2 electrode for flexible high-performance rolling supercapacitor device design. J Mater Chem 2015;3:20973–82. https://doi.org/10.1039/c5ta06265a.

[52] Salunkhe P, Muhammed Ali AV, Kekuda D. Investigation on tailoring physical properties of Nickel Oxide thin films grown by dc magnetron sputtering. Mater Res Express 2020;7. https://doi.org/10.1088/2053-1591/ab69c5.

[53] Zhong S, Sun Y, Xin H, Yang C, Chen L, Li X. NO oxidation over Ni–Co perovskite catalysts. Chem Eng J 2015;275:351–6. https://doi.org/10.1016/j.cej.2015.04.046.

[54] Hardin WG, Slanac DA, Wang X, Dai S, Johnston KP, Stevenson KJ. Highly active, nonprecious metal perovskite electrocatalysts for bifunctional metal-air battery electrodes. J Phys Chem Lett 2013;4:1254–9. https://doi.org/10.1021/jz400595z.

[55] Idriss H. On the wrong assignment of the XPS O1s signal at 531–532 eV attributed to oxygen vacancies in photo- and electro-catalysts for water splitting and other materials applications. Surf Sci 2021;712:2–7. https://doi.org/10.1016/j.susc.2021.121894.

[56] Ji Q, Bi L, Zhang J, Cao H, Zhao XS. The role of oxygen vacancies of ABO3 perovskite oxides in the oxygen reduction reaction. Energy Environ Sci 2020;13:1408–28. https://doi.org/10.1039/d0ee00092b.

[57] Wang HL, Ning XK, Wang ZJ. Enhanced electrical conductivity of Au–LaNiO 3 nanocomposite thin films by chemical solution deposition. RSC Adv 2015;5:76783–7. https://doi.org/10.1039/C5RA15152J.

[58] Ghiasi E, Malekzadeh A, Ghiasi M. Moderate concentration of citric acid for the formation of LaMnO3 and LaCoO3 nano-perovskites. J Rare Earths 2013;31:997–1002. https://doi.org/10.1016/S1002-0721(13)60020-4.

[59] Salman A ul R, Hyrve SM, Regli SK, Zubair M, Enger BC, Lødeng R, et al. Catalytic oxidation of NO over LaCo1−xBxO3 (B = Mn, Ni) perovskites for nitric acid production. Catalysts 2019;9:429. https://doi.org/10.3390/catal9050429.

[60] Flores-Lasluisa JX, Quílez-Bermejo J, Ramírez-Pérez AC, Huerta F, Cazorla-Amorós D, Morallón E. Copper-doped cobalt spinel electrocatalysts supported on activated carbon for hydrogen evolution reaction. Materials 2019;12:1302. https://doi.org/10.3390/ma12081302.

[61] Machado SAS, Avaca LA. The hydrogen evolution reaction on nickel surfaces stabilized by H-absorption. Electrochim Acta 1994;39:1385–91. https://doi.org/10.1016/0013-4686(94)E0003-I.

[62] Hall DS, Bock C, MacDougall BR. Surface layers in alkaline media: nickel hydrides on metallic nickel electrodes. ECS Trans 2013;50:165–79. https://doi.org/10.1149/05031.0165ecst.

[63] Zhang T, Anderson AB. Oxygen reduction on platinum electrodes in base: theoretical study. Electrochim Acta 2007;53:982–9. https://doi.org/10.1016/j.electacta.2007.08.014.

[64] Wang Y, Cheng H. Oxygen reduction activity on perovskite oxide surfaces: a comparative first-principles study of LaMnO 3 , LaFeO 3 , and LaCrO 3. J Phys Chem C 2013;117:2106–12. https://doi.org/10.1021/jp309203k.

[65] Poux T, Napolskiy FS, Dintzer T, Kéranguéven G, Istomin SY, Tsirlina GA, et al. Dual role of carbon in the catalytic layers of perovskite/carbon composites for the electrocatalytic oxygen reduction reaction. Catal Today 2012;189:83–92. https://doi.org/10.1016/j.cattod.2012.04.046.

[66] Osgood H, Devaguptapu SV, Xu H, Cho J, Wu G. Transition metal (Fe, Co, Ni, and Mn) oxides for oxygen reduction and evolution bifunctional catalysts in alkaline media. Nano Today 2016;11:601–25. https://doi.org/10.1016/j.nantod.2016.09.001.

[67] Shinagawa T, Garcia-Esparza AT, Takanabe K. Insight on Tafel slopes from a microkinetic analysis of aqueous electrocatalysis for energy conversion. Sci Rep 2015;5:13801. https://doi.org/10.1038/srep13801.

[68] Bockris JO, Otagawa T. The electrocatalysis of oxygen evolution on perovskites. J Electrochem Soc 1984;131:290. https://doi.org/10.1149/1.2115565.

[69] Ge X, Goh FWT, Li B, Hor TSA, Zhang J, Xiao P, et al. Efficient and durable oxygen reduction and evolution of a hydrothermally synthesized La(Co 0.55 Mn 0.45) 0.99 O 3−δ nanorod/graphene hybrid in alkaline media. Nanoscale 2015;7:9046–54. https://doi.org/10.1039/C5NR01272D.

[70] Bian W, Yang Z, Strasser P, Yang R. A CoFe2O4/graphene nanohybrid as an efficient bi-functional electrocatalyst for oxygen reduction and oxygen evolution. J Power Sources 2014;250:196–203. https://doi.org/10.1016/j.jpowsour.2013.11.024.

[71] Liang H, Hong Y, Zhu C, Li S, Chen Y, Liu Z, et al. Influence of partial Mn-substitution on surface oxygen species of LaCoO3catalysts. Catal Today 2013;201: 98–102. https://doi.org/10.1016/j.cattod.2012.04.036.

[72] Yamashita T, Vannice A. Temperature-programmed desorption of NO adsorbed on Mn2O3 and Mn3O4. Appl Catal B Environ 1997;13:141–55. https://doi.org/10.1016/S0926-3373(96)00099-9.

[73] Silva PRN, Soares AB. Lanthanum based high surface area perovskite-type oxide and application in CO and propane combustion. Eclét Quím 2009;34:31–8. https://doi.org/10.1590/S0100-46702009000100005.

[74] Figueiredo J, Pereira MF, Freitas MM, Órfão JJ. Modification of the surface chemistry of activated carbons. Carbon N Y 1999;37:1379–89. https://doi.org/10.1016/S0008-6223(98)00333-9.

[75] Chubukov BA, Palumbo AW, Rowe SC, Hischier I, Groehn AJ, Weimer AW. Pressure dependent kinetics of magnesium oxide carbothermal reduction. Thermochim Acta 2016;636:23–32. https://doi.org/10.1016/j.tca.2016.03.035.

[76] Cheng J, Navrotsky A, Zhou XD, Anderson HU. Enthalpies of formation of LaMO3 perovskites (M = Cr, Fe, Co, and Ni). J Mater Res 2005;20:191–200. https://doi.org/10.1557/JMR.2005.0018.

[77] Assumpção MHMT, De Souza RFB, Rascio DC, Silva JCM, Calegaro ML, Gaubeur I, et al. A comparative study of the electrogeneration of hydrogen peroxide using Vulcan and Printex carbon supports. Carbon N Y 2011;49:2842–51. https://doi.org/10.1016/j.carbon.2011.03.014.